Icarus 251 (2015) 211–225

Contents lists available at ScienceDirect

Icarus

journal homepage: www.elsevier.com/locate/icarus

Transient bright "halos" on the South Polar Residual Cap of Mars: Implications for mass-balance

Patricio Becerra [a,*], Shane Byrne [a], Adrian J. Brown [b]

[a] Lunar and Planetary Laboratory, University of Arizona, 1629 E. University Blvd., Tucson, AZ 85721, USA
[b] SETI Institute, 189 Bernardo Ave, Suite 100, Mountain View, CA 94043, USA

ARTICLE INFO

Article history:
Received 21 December 2013
Revised 16 April 2014
Accepted 28 April 2014
Available online 9 May 2014

Keywords:
Mars
Mars, polar geology
Mars, polar caps
Ices

ABSTRACT

Spacecraft imaging of Mars' south polar region during mid-southern summer of Mars year 28 (2007) observed bright halo-like features surrounding many of the pits, scarps and slopes of the heavily eroded carbon dioxide ice of the South Polar Residual Cap (SPRC). These features had not been observed before, and have not been observed since. We report on the results of an observational study of these halos, and spectral modeling of the SPRC surface at the time of their appearance. Image analysis was performed using data from MRO's Context Camera (CTX), and High Resolution Imaging Science Experiment (HiRISE), as well as images from Mars Global Surveyor's (MGS) Mars Orbiter Camera (MOC). Data from MRO's Compact Reconnaissance Imaging Spectrometer for Mars (CRISM) were used for the spectral analysis of the SPRC ice at the time of the halos. These data were compared with a Hapke reflectance model of the surface to constrain their formation mechanism. We find that the unique appearance of the halos is intimately linked to a near-perihelion global dust storm that occurred shortly before they were observed. The combination of vigorous summertime sublimation of carbon dioxide ice from sloped surfaces on the SPRC and simultaneous settling of dust from the global storm, resulted in a sublimation wind that deflected settling dust particles away from the edges of these slopes, keeping these areas relatively free of dust compared to the rest of the cap. The fact that the halos were not exhumed in subsequent years indicates a positive mass-balance for flat portions of the SPRC in those years. A net accumulation mass-balance on flat surfaces of the SPRC is required to preserve the cap, as it is constantly being eroded by the expansion of the pits and scarps that populate its surface.

1. Introduction

The polar regions of Mars contain some of the most geologically young surfaces on the planet, as well as its largest reservoirs of water and carbon dioxide ice. The deposition and erosion of these icy surfaces is intimately linked to climate (Byrne, 2009). Therefore, the study of the geology and geomorphology of Mars' poles can provide important information about the planet's recent climatic history and inter-annual variation.

At the South Pole, a permanent layer of high-albedo CO_2 ice exists that survives the summer sublimation of the seasonal CO_2 caps (Leighton and Murray, 1966), known as the South Polar Residual Cap (SPRC) (Kieffer, 1979). This CO_2 ice cap varies in thickness from approximately 2 to 10 m (Byrne and Ingersoll, 2003; Thomas et al., 2000), and is concentrated between 84°S and 89°S latitude, and between 220°E and 50°E longitude. The SPRC contains a large number of erosional scarps and flat-floored, quasi-circular pits embedded in its ice slabs (initially described by Thomas et al. (2000) and informally known as "Swiss-cheese terrain" (Malin and Edgett, 2001) because of their appearance when observed from orbit). The depths that these features have eroded into the SPRC ice slabs range from less than a meter up to ten meters, and in some places allow the water ice underlying the SPRC to show through (Bibring et al., 2004; Byrne and Ingersoll, 2003; Titus et al., 2003).

Thomas et al. (2005, 2009) performed a detailed geologic mapping of the SPRC using images acquired by the Mars Global Surveyor (MGS) Mars Orbiter Camera (MOC) (Malin and Edgett, 2001), and the High Resolution Imaging Science Experiment (HiRISE) (McEwen et al., 2007) aboard the Mars Reconnaissance Orbiter (MRO). They identified four distinct depositional units, each with characteristic erosional patterns, and with different total surface coverage over the SPRC (Fig. 1 in Thomas et al. (2009)). The inclined walls of the erosional pits in all of these units retreat by 2–4 m per martian year, depending on the particular depositional unit (Malin et al., 2001; Thomas et al., 2009). This erosional

* Corresponding author.
E-mail address: becerra@lpl.arizona.edu (P. Becerra).

http://dx.doi.org/10.1016/j.icarus.2014.04.050
0019-1035/

evolution seems to suggest that the SPRC is in the process of disappearing, and that the martian climate is changing (Malin et al., 2001). In fact, based on these retreat rates, and the spatial density of the pits, the entire SPRC should disappear within about a century. However, a landscape-evolution model (Byrne, 2011) has been suggested for the SPRC, in which pits form spontaneously due to imbalances in the energy budgets of different areas of the surface, caused by intrinsic surface roughness. This model does not require climate change, but instead necessitates ongoing accumulation of ice on flat surfaces with inter-annual variability in the deposition rate in order to form a recurring SPRC.

Unlike the retreat rates of sloped surfaces such as pit walls, the mass-balance of flat surfaces on the residual cap is extremely difficult to measure from images, so we must rely on the analysis of changing brightness patterns in order to extract information from the flat inter-pit mesas. Here we report on ephemeral albedo features that appeared on the SPRC immediately after a midsummer global dust storm: a large number of the pits and scarps characteristic of the SPRC were seen to exhibit a bright decameter-scale "halo" around their edges (Fig. 1). These albedo halos appeared during the southern-summer of Mars year (MY) 28, at $\sim L_s$ 270–280° (L_s is solar longitude, it is used to measure the time of year on Mars, and it represents the position of the planet in its orbit relative to north vernal equinox, defined as $L_s = 0°$; according to the convention of Clancy et al. (2000), MY 1, began on April 11th, 1955), and disappeared later that same summer between L_s 330° and 340°. We observed the halos on all geologic units mapped by Thomas et al. (2009), although their appearance and intensity differed slightly from one unit to another. The most easily visible and measurable halos were seen in Unit B (Fig. 1a–d and g in this paper; Figs. 10c and 15b in Thomas et al. (2009), also display noticeable halos). The halos were observed only during one out of eight Mars years for which observations at high enough resolution exist.

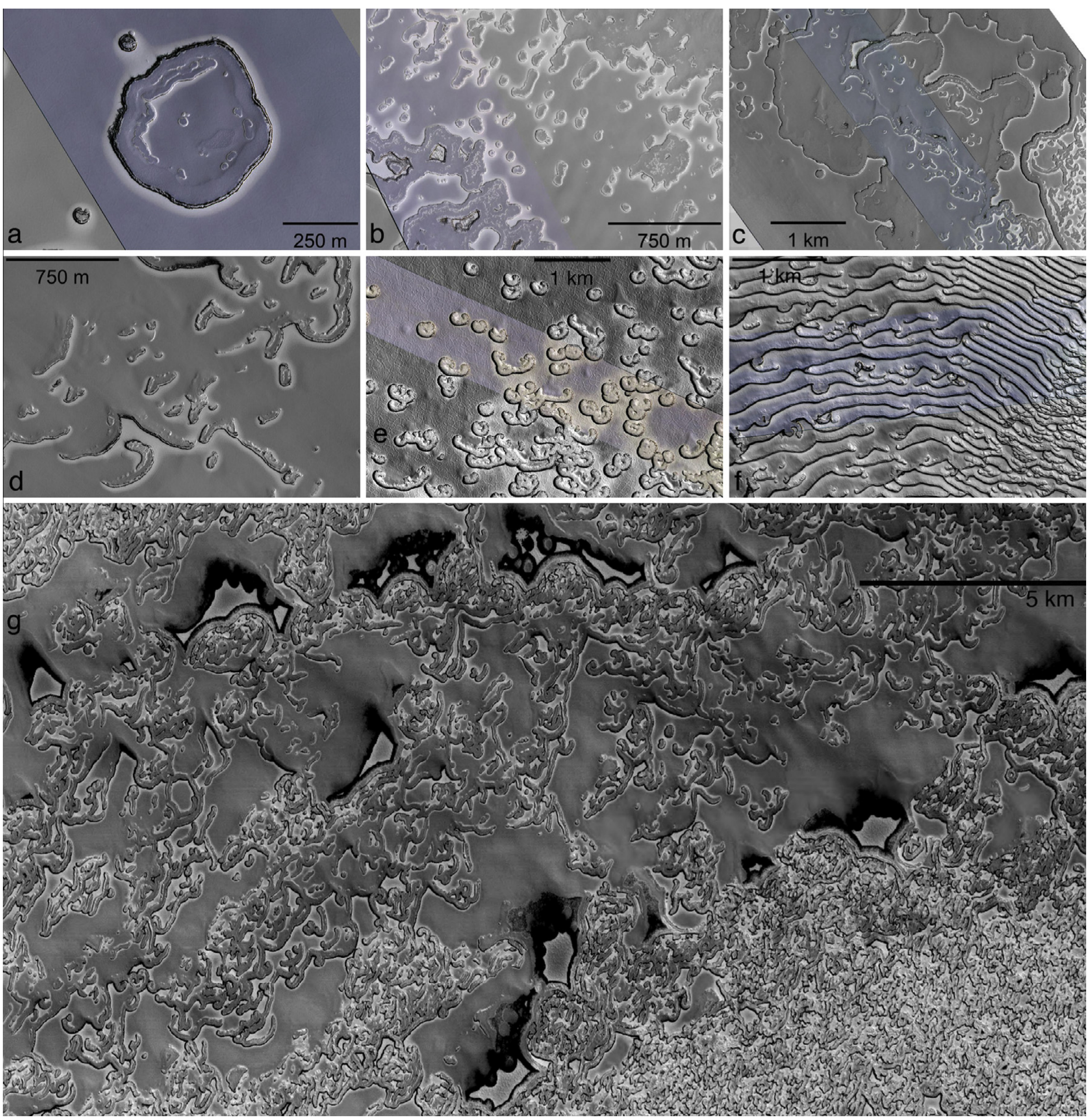

Fig. 1. Examples of HiRISE (a–f), and CTX (g) images of eroded terrain on the SPRC exhibiting halos. (a–d) PSP_004989_0945, PSP_005002_0945, PSP_004765_0940, PSP_004858_0940. Halos on Unit B of Thomas et al. (2009). (e) PSP_005043_0930. Unit A1 displayed faint halos that were difficult to measure because of comparable brightness changes in the terrain due to small-scale topographic relief. (f) PSP_005576_0940. Fingerprint terrain in Unit A2, showing a faint brightness difference between areas close to the edges of the scarps, and areas farther away. (g) P11_005227_0937_XN_86S003W. Larger-scale CTX image of a halo-covered region. Halos are visible on the isolated mesas of Unit A0, and around the smaller pits and depressions of Unit B.

This particular year, MY 28, was marked by a global dust storm that began near Mars' perihelion (L_s 252°), in the middle of southern summer. The timing of the halos suggests that their appearance could have been related to this event, which affected the overall mass balance of the SPRC. These anomalous dust-storm years are expected to result in increased overall ablation of the SPRC (Bonev et al., 2008), but they have also been suggested to play an important role in the preservation of the residual cap through the reduction of surface roughness by increased snowfall replacing direct freezing of ice onto the surface (Byrne, 2011). Hayne et al. (2014) have shown that snowfall is consistent over the SPRC during winter, and contributes between 3% and 20% by mass of the seasonal CO_2 deposition. In addition, the amount and importance of snowfall for newly deposited ice is probably variable from year to year, as there is evidence that cold spot activity in the south polar cap can be affected by global dust storms (Cornwall and Titus, 2010).

We present results from an observational analysis of the SPRC halos that were obtained through the examination of spacecraft data in combination with a reflectance model of the SPRC surface based on Hapke theory (Hapke, 2012). Our goal is to provide a thorough characterization of these features, detailing their size, shape, location, time of appearance and disappearance, composition, and dependence on insolation, as well as to hypothesize a formation mechanism and describe the implications of their existence on the mass-balance of the SPRC.

We have demonstrated that the effects of a near-perihelion global dust storm on the residual cap are significant, and such events do not happen regularly. The study of the halos' transient existence helps characterize the mass balance of the SPRC during such anomalous years, providing valuable insight that could help explain the cap's persistence in the martian south-polar region.

2. Methods

2.1. Image datasets

The primary objective of our image analysis was to constrain the timing and location of halos on the residual cap. For this purpose we performed a survey and analysis of data from three imaging instruments: the Narrow Angle Camera of the Mars Orbiter Camera (MOC) on Mars Global Surveyor (MGS), the High Resolution Imaging Science Experiment (HiRISE), and the Context Camera (CTX) (Malin et al., 2007), both on board the Mars Reconnaissance Orbiter (MRO).

Due to its large image swath ($\sim$30 $\times$ $\sim$160 km) and high-resolution (6 m/pixel) widespread coverage of the martian south-polar region (Malin et al., 2007), the CTX dataset was used initially to search for evidence of halos throughout the SPRC. CTX has achieved nearly 100% coverage of the SPRC each year between MY 28 and 31. During our search we used CTX images from all available years to check the entire surface of the SPRC looking for halo-covered regions in which the SPRC material displayed noticeable brightening on the edges of erosional pits and scarps (Fig. 1g).

After the initial CTX survey, we used the sparser, but higher resolution data of HiRISE and the MOC Narrow Angle Camera to observe certain regions of the cap more closely, and select specific pits in smaller areas that are best suited for further analysis and characterization. HiRISE has a maximum resolution of 25 cm/pixel, and an image swath width in its RED detector of 5 km from an altitude of 250 km, which make it optimal for examining meter to decameter-sized surface features. Most importantly, the relative uncertainty between two pixel values in one image is less than 2%. Therefore, it is ideal for a thorough analysis of minor brightness differences such as the halos. HiRISE acquires images using three detectors that correspond to three color bands: The blue–green (BG) band (400–600 nm), the RED band (550–850 nm), and the Near Infrared (NIR) band (800–1000 nm) (McEwen et al., 2007; Delamere et al., 2010). The MOC Narrow Angle Camera has a spatial resolution of up to 1.4 m/pixel and a swath width of up to 2.9 km, with a single panchromatic band (Malin and Edgett, 2001). Our complete dataset comprises 732 HiRISE images spanning four southern springs and summers from MY 28 to 31, between L_s 180° and 360°, and 175 MOC images from MY 24–27 over the same L_s range that overlap areas in which HiRISE and CTX observed halos.

Based on our survey of these datasets, we selected 9 sites on the SPRC on which to perform a quantitative observational analysis. These sites were chosen based primarily on the temporal density of imaging coverage in the area, with consideration given to sampling a wide longitudinal range. In addition, we eliminated sites with terrain where it would have been difficult to measure halo properties, such as polygonal troughs in the flat surroundings (as in Unit A1 of Thomas et al. (2009), Fig. 1e), or closely spaced parallel scarps where, although halos were present, they were difficult to distinguish from the underlying geomorphology (as in Unit A2, Fig. 1f). The locations of our selected sites are shown in Fig. 2, and their informal names and geographic coordinates are listed in Table 1.

We examined the images using the map-projection tools of the Java Mission-planning and Analysis for Remote Sensing (JMARS) geospatial information system (GIS), developed by the Mars Space Flight Facility at Arizona State University. This suite of software tools allowed us to easily search for overlap between the various datasets, simultaneously search different Mars years of observation with one or more datasets, and map-project the images onto wide-angle mosaics in order to easily locate the areas of the cap that we were examining and constrain a location for the appearance of halos.

2.2. Width, brightness, and color measurements of selected halos using HiRISE

HiRISE images at our chosen study sites were analyzed in order to extract quantitative information about the brightness and size of the features we identified as halos, and how these properties vary with time of year, position on the cap, and aspect of the adjacent pit walls with respect to north. We imposed an important criterion in order for an observed scarp-adjacent brightness difference to be classified as a halo: the brightness difference was required to be present adjacent to walls oriented at any and all aspects with respect to north, within one image. This excludes brightness changes that represent a different phenomenon than the halos. For example, an albedo rise on the ice adjacent to the sun-facing walls of a pit that is absent next to the sun-opposing walls suggests that it is most likely due to a slight inward dip of the surrounding surface as it approaches the edges of the walls, and is not, like the halos, a feature that is independent of the morphology of pit edges. We have observed this inward dip of the ice around the majority of erosion features on the SPRC.

Once we had selected specific halos for analysis, we used Exelis Visual Information Solutions' Environment for Visualizing Images (ENVI) to measure the width and maximum brightness of the halos. We extracted one-dimensional profiles of I/F values (measured intensity (I) divided by the solar irradiance when the incidence angle is zero (F), such that $I/F = 1$ for a perfectly diffuse reflector that is normally illuminated) from the edge of a pit or scarp on a HiRISE image, out to a point within the surrounding plateau that appeared to have a uniform brightness. These I/F values were then converted to Lambert Albedo (A_L) by dividing them by the cosine of the incidence angle. We plotted A_L of the HiRISE

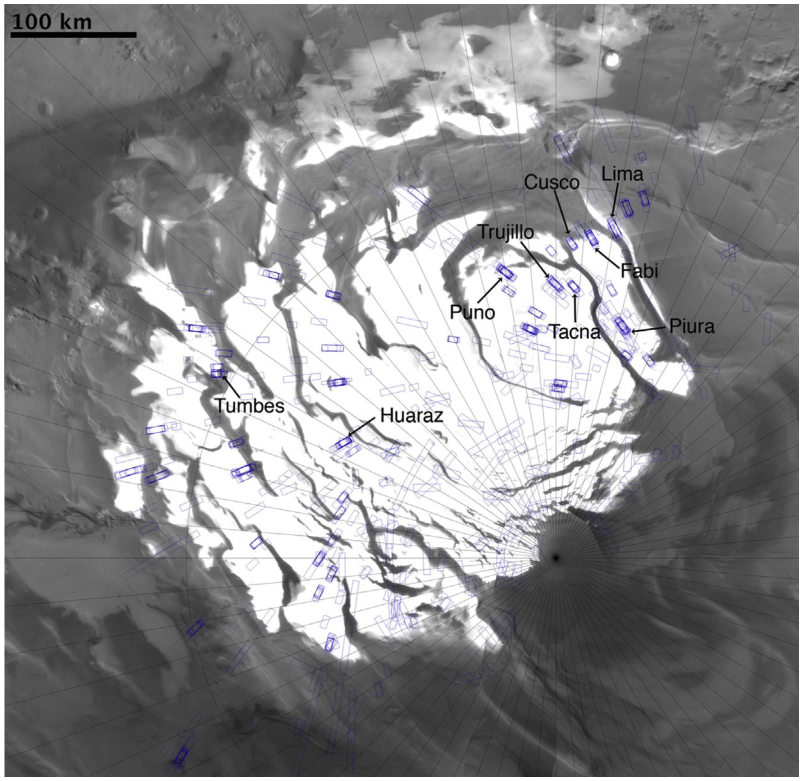

Fig. 2. MOC Wide Angle Camera Mosaic of the SPRC with HiRISE image stamps superimposed (blue rectangles). Meridians and parallels are spaced every 5°. The zero Meridian is pointing upward. The locations of the sites selected for analysis along with their informal names are shown. (For interpretation of the references to color in this figure legend, the reader is referred to the web version of this article.)

Table 1
List of sites selected for detailed analysis. The left three columns list the informal names given to the sites, and their center latitude and longitude. The right two columns list the number of HiRISE images taken in MY 28 between L_s 279° and 331°.

Site name	Center latitude	Center longitude	# of HiRISE MY 28 images	L_s of images with halos, 279° < L_s < 340°
Trujillo	−86.3	0.1	3	286, 303, 331
Cusco	−85.7	2.8	2	288, 298
Tacna	−86.3	3.6	2	283, 323
Fabi	−85.7	6.3	2	288, 298
Lima	−85.5	10.2	4	285, 299, 309, 315
Piura	−86.7	15.4	1	284
Tumbes	−84.8	298.8	2	320, 325
Huaraz	−86.7	297.8	2	293, 317
Puno	−86.1	350	4	282, 289, 292, 315

RED band against distance away from the scarp edge, and fit a Gaussian curve to the brightness profile (Fig. 3). Using these fits, we measured the peak value (representative of the maximum halo brightness), and the full width at half maximum of the Gaussian (representative of the halo width from the edge of the wall). This process was repeated for different orientations of scarp walls in an image, ranging from 0° aspect, meaning that the wall faces north, to 360°, in intervals of approximately 30°. For this reason, near-circular pits like the one at Fabi (Fig. 3) were preferred over irregular erosion patterns such as those seen in parts of sites Cusco (Fig. 1c) and Puno (Fig. 1d), due to the fact that the former contained all pit wall aspects in equal abundance and from a single pit.

In order to look for differences in color between areas close to pit walls, where the halos were seen, and areas farther away, we used A_L profiles taken from all three HiRISE bands. Ice with deposited atmospheric dust will have a lower albedo at BG wavelengths than at RED wavelengths. Therefore, a lower BG/RED ratio signifies a dustier section of the ice, whereas a higher ratio implies a lower amount of dust contamination for that area (Delamere et al., 2010).

2.3. CRISM spectral data analysis

In order to compare the composition of the ice in the halos with that of the surrounding SPRC surface, we examined data products acquired by MRO's Compact Reconnaissance Imaging Spectrometer for Mars (CRISM) (Murchie et al., 2007). In particular, we used spectra from the CRISM IR array, which samples a wavelength range from 1.0013 μm to 3.9368 μm in 438 channels (6 nm sampling). Our goal with the spectral analysis was twofold: 1. Test for the presence of contaminants such as water ice and/or dust within the CO_2 ice, which could be responsible for the albedo difference observed at the halos. 2. Examine the difference in band depth of characteristic CO_2 bands between the halos and the plains, and use this as a proxy for relative CO_2 ice grain size, to determine whether the albedo difference could be caused by a difference in ice grain size.

To explore compositional differences, we compared a spectrum taken from a pixel within a halo with one taken from the surrounding plains. We looked for two absorption bands in the spectra that are typically used as a diagnostic to determine the presence of CO_2

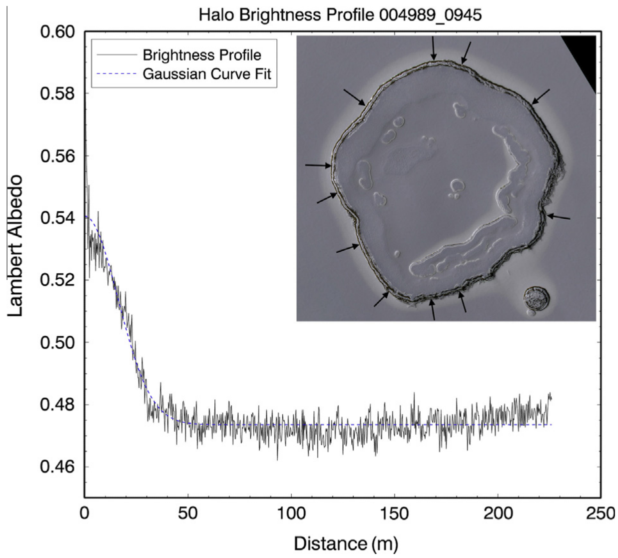

Fig. 3. Example of a brightness profile taken from the "Happy Face" pit at the Fabi site (PSP_004989_0945). The circular shape of this pit allowed profiles to be taken at every possible orientation of the pit walls (top right corner – large pit diameter is ~500 m). The plot shows the Lambert albedo of a brightness profile in the HiRISE RED band vs. distance from the edge of the scarps. We fit a Gaussian curve and determined the maximum brightness and the width of the halo (FWHM) for each profile on every image analyzed.

ice. These are centered at 1.435 μm (shoulder points at 1.38 and 1.47 μm), and at 2.28 μm (shoulder points at 2.2 and 2.4 μm). To determine whether or not water ice was present as a significant contaminant, we looked for two IR bands that are characteristic of water ice, centered around 1.5 μm and 3.0 μm.

We assumed dust to have the atmospherically derived spectrum from Wolff et al. (2009); this dust has a strong effect on the visible albedo, but is spectrally neutral in the near IR. Therefore we based our estimates of dust presence on the measurements of HiRISE color ratios interpreted through our spectral model, which is presented in the following subsection.

Spectral band depths are a measure of absorption, and can be used to determine ice grain sizes. We measured the 1.43 μm band depth following the formula given in Clark and Lucey (1984), which normalizes the reflectance of the band (R_b) and the spectral continuum (R_c), to the spectral continuum: $(R_c - R_b)/R_c$. We utilized this quantity as a proxy for ice grain size, measuring it in areas adjacent to pit edges where halos were seen, and in areas distant from the pits. We calculated the band depth throughout CRISM IR images taken at the time of the halos, and constructed band depth maps that show the value of the specified band depth at each pixel. These maps were then used to compare these values at different parts of the CRISM image, in particular, comparing pit-adjacent band depths to surrounding band depths.

2.4. Hapke reflectance model

We constructed a surface reflectance model based on Hapke reflectance theory (Hapke, 2012) in order to find ice compositions and grain sizes that could self-consistently explain the albedos, colors, and spectral features of the halos. Our model primarily followed the examples of Roush (1994), and Warell and Davidsson (2010), and neglected atmospheric extinction and scattering. We used this model, along with the HiRISE (Delamere et al., 2010) and CRISM (Murchie et al., 2007) band-pass coefficients to simulate HiRISE brightness in each band and CRISM spectra. We attempted to reproduce the reflectance of a particulate mixture of CO_2 ice, water ice, and dust that would match the HiRISE RED channel Lambert Albedo, HiRISE BG/RED color ratio, and CRISM 1.43 μm band depths observed at the halos and in the surrounding SPRC ice. The principal equations and assumptions needed for the implementation of our model are discussed in more detail in Appendix A. An in-depth description of Hapke theory can be found in Hapke (2012).

We used as few free parameters as possible to simulate the spectrum, so our model consists of a combination of only carbon dioxide ice, water ice, and dust (and their independent grain sizes) in an intimate mixture. The real and imaginary indices of refraction of H_2O ice were taken from Warren (1984), CO_2 ice indices were obtained from Hansen (2005), and dust indices from Wolff et al. (2009).

The model outputs I/F between 0.35 μm and 4 μm, at a resolution of 1 nm. After convolution with the instrument response curves, we obtain simulated I/F values for all three HiRISE bands and for all CRISM wavelengths in both the CRISM S (shortwave 0.3–1 μm), and L (1–4 μm) channels (see Appendix A). Finally, we use these I/F values to calculate HiRISE RED A_L (dividing by the cosine of the incidence angle), HiRISE BG/RED ratio, and CRISM 1.43 μm band depths. We ran the model for incidence angles of 65°, 70°, 72°, and 75°, which are representative of the incidence angles of the images we selected for analysis (varying the incidence angle within this range had negligible effects on the results).

3. Observations and results

3.1. Timing and location of halos

Our initial survey of images of our selected sites taken over 8 Mars years, described in Sections 2.1 and 2.2, showed that halos were only present on the SPRC during a small portion of southern summer in MY 28 (Figs. 4, 5, S1, and S2 in the Supplementary material). Although several images on MY 30 and 31 displayed an increase in brightness on flat areas adjacent to sun-facing pit walls compared to the surrounding plains (Fig. 4 shows two examples of this on MY 30, L_s 300°, and on MY 31, L_s 288°), these albedo rises did not fit the halo criterion explained in Section 2.2 and can instead be attributed to inward dipping terrain near the pit wall. These examples were therefore not counted as halos.

The earliest that halos appeared in MY 28 was L_s 279°, which seems to coincide with the time that the pit walls begin to defrost, exposing older, darker ice layers (Fig. 4). With increasing L_s, the halos grew in width and relative brightness difference to their surroundings. By L_s 290°, most large mesas on the cap displayed prominent halos around the edges of the erosional depressions. Although the overall albedo of the entire SPRC, including the halos, darkened with time, the relative difference between the albedo of the halos and that of the surrounding ice increased (Fig. 5).

The timing of disappearance of the halos was between L_s 325° and 331° (Figs. 4 and 6). The earliest MY 28 images that did not show any halos in locations where they had been observed previously were taken in L_s 325°; and the longest-lived halos were observed in an image taken on L_s 331°. Fig. 6 is a plot of the temporal distribution of all HiRISE and MOC images that we examined, and it clearly shows that the "halo season" of MY 28, between L_s 279° and 331°, is the only time when we observed halos in the data. This observation of a restricted timing for the existence of these features reduced our dataset in the 9 selected sites to 22 HiRISE images taken during this season, on which we performed the detailed analysis described in Section 2.2. The corresponding site name and solar longitude of acquisition of these images is shown in the two rightmost columns of Table 1.

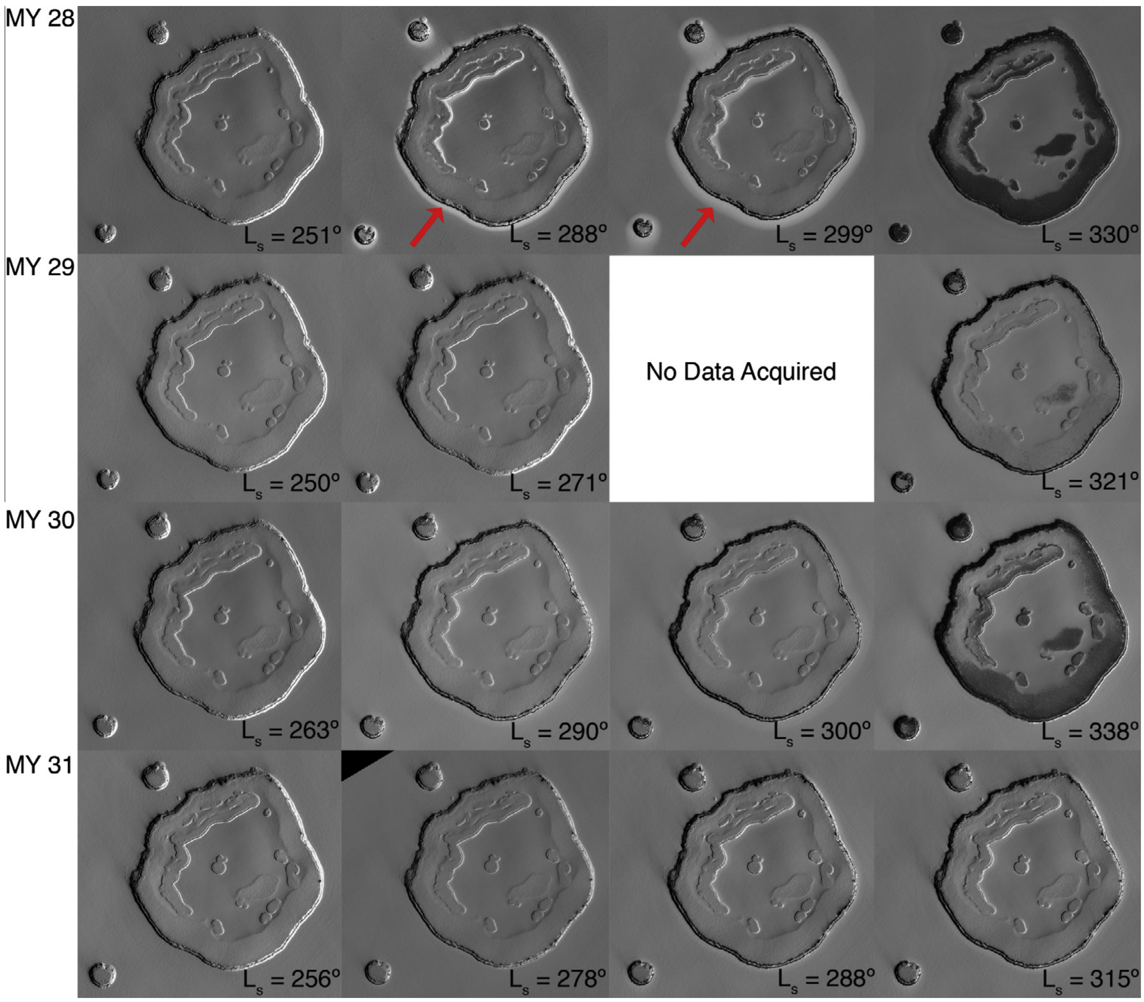

Fig. 4. "Happy Face" pit at the Fabi site imaged by HiRISE at four different times of year during MY 28 (PSP_004000_0945, PSP_004778_0945, PSP_004989_0945, PSP_005701_0945), MY 29 (ESP_012808_0945, ESP_013243_0945, ESP_014311_0945), MY 30 (ESP_021880_0945, ESP_022447_0945, ESP_022658_0945, ESP_023515_0945), and MY 31 (ESP_030570_0945, ESP_031005_0945, ESP_031216_0945, ESP_031796_0945). Red arrows in the top two center panels denote the halos around this pit. On MY 28, the halo is first observed on L_s 288°, which appears to be the time the pit walls begin to defrost. It is visible on L_s 299°, and is no longer visible at L_s 330°. We did not observe halos on the SPRC in images from any other MY. (For interpretation of the references to color in this figure legend, the reader is referred to the web version of this article.)

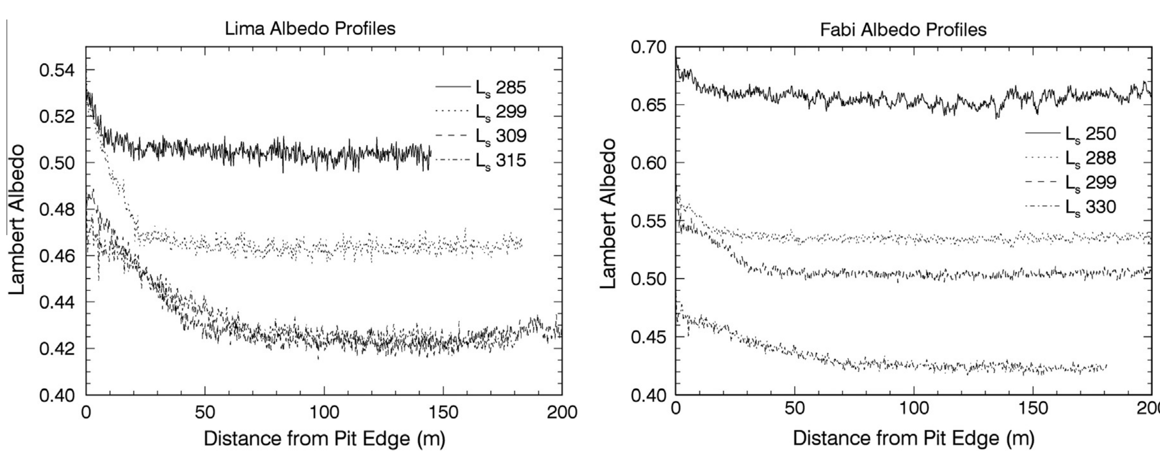

Fig. 5. Temporal changes in the MY 28 albedo profiles taken from two of our selected sites. The profiles shown here for each of the two sites were measured from the same orientation of the scarp wall, during different times of the year. The Lima site (left) had more frequent HiRISE coverage during the time of the halos, so the growth in width and relative brightness difference is more easily visible. The Fabi site (right) displays the large drop in the albedo of SPRC from before the dust storm (L_s 250°) to after the dust storm when halos were already present (L_s 288°). These profiles were taken from a sun-facing wall, so a slight increase in albedo close to the walls is visible even when the halos were not present (L_s 250°, 330°).

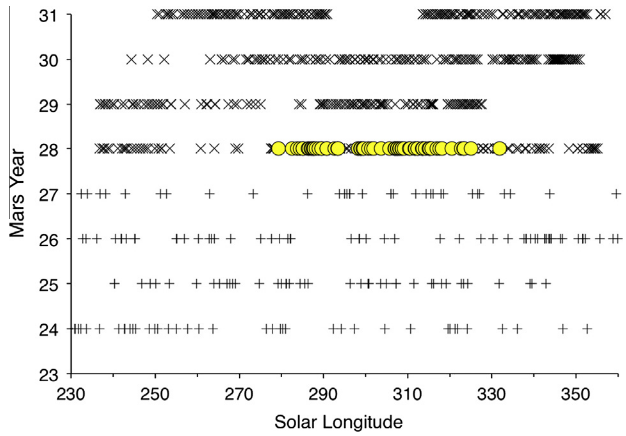

Fig. 6. Temporal distribution over MY and L_s of all HiRISE (X) and MOC (+) images examined. The yellow dots represent those images in which halos were seen. The gap in observations at L_s 330–360° in MY 29 was due to MRO going into safe mode, and the gap at L_s 290–315° of MY 31 was due to solar conjunction.

3.2. Width and brightness of halos

Halos in all images of our selected sites were examined using the method described in Section 2.2. All analyzed sites displayed similar behavior, and selected results of our observations are shown in Figs. 7 and 8. These figures show the variation of halo width and maximum brightness with orientation of the scarp wall.

The average width of the halos ($\pm 2\sigma$) is 12.14 ± 1.44 m during L_s 280–295°, 32.96 ± 4.02 m at L_s 295–305°, and 55.48 ± 6.98 m at L_s 305–340°. In 16 of the 22 images, the widest halos were observed adjacent to the edges of equator-facing (north-facing) scarps (Fig. 7), while four cases showed the widest sections adjacent to sun-facing walls, and two cases adjacent to other wall orientations.

Fig. 8 shows the dependence of maximum brightness with orientation. In general ($\pm 2\sigma$) the halos were 4 ± 0.3% brighter than the surroundings during L_s 285–295°, 7 ± 0.7% brighter between L_s 295–305°, and 8 ± 0.6% brighter at L_s 305–330°. In all images, the brightest portions of the halos were observed adjacent to sun-facing walls. However, images of these sites before and after the halos in MY 28, and in later years when the halos were not present, show a similar relationship between terrain brightness and solar azimuth, indicating that this trend could be due to the inward sloping of the surface close to the edges of the pits, and not a property of the halos themselves.

3.3. Composition and grain size

The albedo differences observed between the halos and the surrounding SPRC terrain may be caused by differences in the amount of impurities within the CO_2 ice, by differences in the ice grain size, or by other effects upon the surface photometric function, such as sub-pixel and supra-grain-size textures. Therefore, the composition of the halos constrains the processes that could have led to their appearance. If the halos and the surrounding SPRC plains are composed of essentially pure CO_2, then a difference in the grain sizes of the ice must be responsible for their brighter appearance. However, if water–ice impurities and/or a higher degree of dust contamination are present in the surroundings, then these impurities are more probable explanations for the observed albedo contrast.

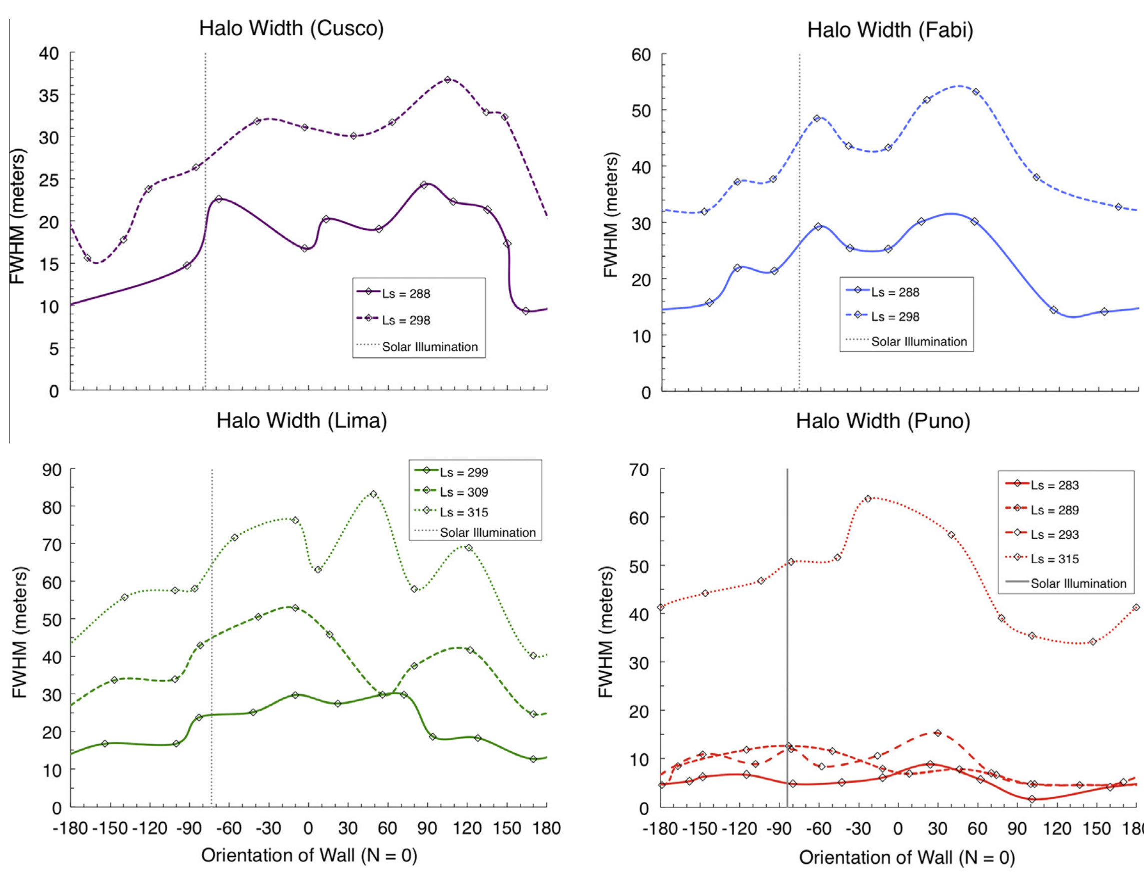

Fig. 7. Variation of the width of halos with orientation of the pit walls (north-facing wall = 0°) for pits on four selected sites on the SPRC. The halos appear wider on the edges of equator-facing walls.

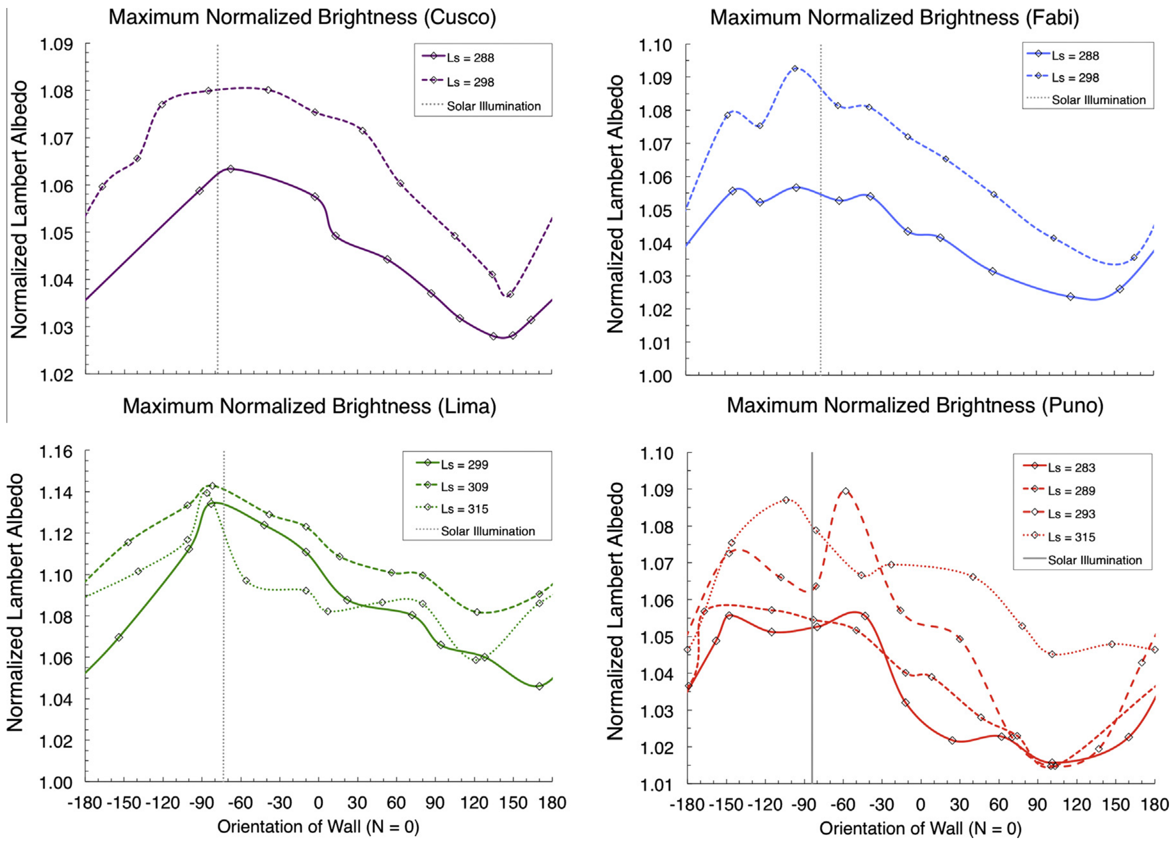

Fig. 8. Variation of the maximum brightness of the halos with orientation of the pit walls (north-facing wall = 0°) for pits on four selected sites on the SPRC. The albedo has been normalized to the average brightness of the flat terrain distant from the pit walls. The brightest sections of the halos appear to be on the edges of sun-facing walls.

Fig. 9a shows two CRISM spectra from Fabi at L_s 299°, when the halos were observed in the HiRISE data. Spectra taken from areas near scarp walls (0–40 m) were compared to those taken from regions relatively far from the walls (100–500 m) in the surrounding plateaus (Fig. 9b). The spectra from both areas show the same general shape and display the characteristic absorption bands of CO_2 ice at 1.435 μm and 2.28 μm. In addition, the complete absence of the broad water ice absorption bands at 1.5 μm and 3.0 μm, rule out any contamination by H_2O larger than 1% by volume (Brown et al., 2010, 2012).

Could this albedo difference be a product of grain size differences in the CO_2 ice? Smaller ice grains absorb less light and therefore appear brighter than larger ice grains. The band depths of the CO_2 ice absorption features for the ice within the halos were measured to be around 0.4 (1.435 μm) and 0.12 (2.28 μm). According to Fig. 2a and b from Brown et al. (2010), this corresponds to 3–5 mm spectroscopic grain sizes for CO_2 ice. Fig. 9c shows a band depth map of the portion of the Fabi site displayed in 9b. Similar maps were made for all selected sites at all available observation times. The maps display a range of band depths, corresponding

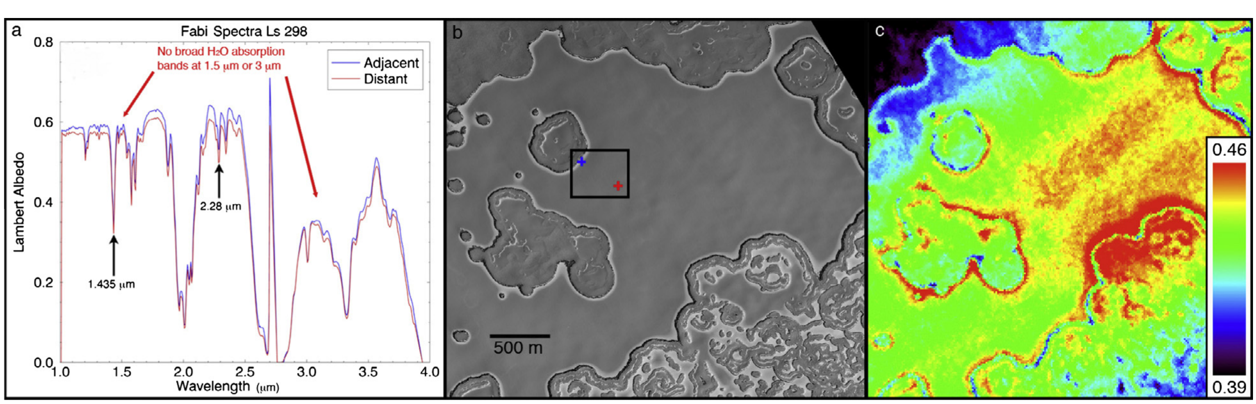

Fig. 9. (a) CRISM IR spectra of halos (adjacent, blue), and surrounding plains (distant, red) on the Fabi site at L_s 299°. Spectra were taken from individual pixels of CRISM image (FRT00007353). The 1.435 μm and 2.28 μm absorption bands characteristic of CO_2 ice are indicated. No evidence of water ice is observed, as evidenced by the lack of broad 1.5 μm and 3.0 μm absorption bands (Brown et al., 2010). (b) HiRISE image of the Fabi sit at L_s 299° (PSP_004989_0945). The blue and red crosses within the box indicate the specific locations from which the spectra in (a) were taken. (c) 1.43 μm band depth map of the same CRISM image from (a). Higher (redder) values correspond to deeper bands, which imply larger CO_2 ice grains. In general, the locations of the halos seen in (b) have deeper band depths than their surroundings.

to a range of grain sizes. In general, our band depth maps display deeper bands wherever halos are observed in the corresponding HiRISE image. This means that the halos are not systematically smaller grained than their surroundings, which is what we would expect if the mechanism that caused them were simply a grain size difference in the ice. We cannot say that the halos are systematically larger-grained, since the maps displayed deep bands in other areas of the image, and showed complicated band depth patterns. The map in Fig. 9 in particular has an overall tendency for high band depths in a diagonal band across the image (bottom left to top right). However, this is an artificial effect caused by the presence of a dark band in the center of CRISM images that is a result of gimbal rotation, and should be ignored. Based on our observations of higher band depths corresponding to halo locations across all sites, we can confidently conclude that the albedo difference observed as halos was not caused by the presence finer grained frost.

To test for a dust-driven albedo difference we looked at color differences in the HiRISE data. Color ratio profiles for sites Fabi and Lima are shown in Fig. 10. We found that 8 out of our 9 study sites (especially those with well-developed halos later in the season) had a 0.5% to up to 4% increase in the BG/RED ratio close to the walls. This rise in "blueness" approximately coincided with the width of the observed halos, which makes the halos consistent with dust deficits.

3.4. Reflectance model results

The principal objective of our Hapke model was to explore the possibility that small differences in dust content between two areas of the cap could give rise to comparatively large differences in albedo, such as those manifested in the halos.

As water ice in the SPRC was ruled out by the CRISM observations, this component, although built into our model, was not included in the surface reflectance simulations. Thus, the free parameters in the model are: 1. Grain size of CO_2 ice particles. 2. Grain size of dust particles. 3. Volumetric dust content. We ran the model for the following parameter space: CO_2 grain sizes ranging from 0.5 mm to 50 mm, dust volumetric content ranging from 0% dust (i.e. pure CO_2 ice), to 1% dust, and dust grain sizes ranging from 1 to 20 μm. We assumed isotropic scattering from the surface (see Appendix A), and neglected all atmospheric contributions on

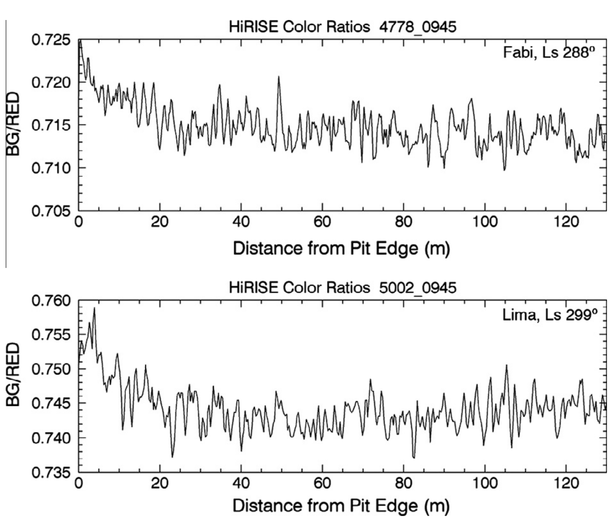

Fig. 10. HiRISE BG/RED profiles for sites Fabi and Lima. Most sites showed at least a 1% increase in this color ratio at the halo locations with respect to the surrounding terrain.

the scattering of sunlight. Atmospheric scattering can change the albedo and color of the terrain observed, but its effect is not expected to differ over short length scales. This modeling effort is restricted to comparing halos to adjacent terrain, and assumes the atmosphere has affected both terrains equally. The absolute values reported in Table 2 should therefore be interpreted with caution; however, the relative differences between halo areas and their surrounding terrain (i.e. the fact that halos are areas with less dust) are robust.

To compare the measured values from spacecraft observations with the model output, we plotted all modeled RED A_L, BG/RED, and CRISM 1.43 band depths as a function of dust volume content and CO_2 ice grain size as a contour map for a particular dust grain size, and then shaded the region between those contours that matched the observed values for each site at the halo and at the surrounding ice (Fig. 11). The shaded areas were changed to match the observed values at each time of year for each site. In many cases there was no self-consistent solution that could simultaneously explain the albedos, colors and band depths of the halos for a particular dust grain size. We therefore varied the dust grain size between 1 and 20 μm and found that solutions were only possible for dust grain sizes between 10 and 20 μm depending on the time of year. Fig. 11 illustrates the range of dust contents and CO_2 grain sizes that, with a grain size of 15 μm, simultaneously explain the albedo, color, and band depths observed at site Lima at L_s 299°. Our results for sites Cusco, Fabi, and Lima are shown in Table 2. We will use Lima as the prototype site to explain these results, as it has the most temporally dense HiRISE and CRISM coverage over the halo season.

The model shows a decrease in albedo as higher dust contents are added, and is able to identify a self-consistent set of parameters that together define the composition of the SPRC surface at the time of the halos. The model values that match the observations indicate that a dust difference of just a few hundredths of a percent by volume can give rise to the higher albedos seen at the halos. For instance, at L_s 300° (Fig. 11) the parameters found to replicate the observations at Lima are CO_2 grain sizes of 8–10 mm, dust grain sizes of 14–17 μm, and a difference in dust content of 0.02% between halos and surroundings. At L_s 310°, when the halos are most prominent in the Lima site, the dust content is 0.05% at the halos, and 0.08% at the surrounding areas. The dust content seems to increase with L_s, indicating that more dust is being deposited as time passes. This is true both within the halos themselves and over the rest of the SPRC, but the halos are always found to have smaller dust contents than their surroundings. This agrees with observations that show all SPRC surfaces getting darker with time, but the halos darkening more slowly (Fig. 5).

4. Discussion

4.1. Implications of results

Analysis of the HiRISE profiles allowed us to obtain important measurements that characterize the SPRC halos. We observed that the halos have widths of decameters and are widest when adjacent to equator-facing (north-facing) walls. At areas close to the South Pole (~87°S), north-facing slopes spend more time in the sunlight than equivalent south-facing slopes, so that cumulative insolation is greater for the former. The fact that in most cases the widest sections of halos are adjacent to north-facing walls, points to a connection between halo formation and insolation. The time of appearance of the halos also supports this argument, as it was observed to coincide with the defrosting of the pit walls (Fig. 2), which leads to a jump in sublimation rates because of the sudden decrease in albedo of the walls. In addition, the time at which the

Table 2
Hapke model results of the free parameter combinations that matched the observed values of albedo (HiRISE RED), color (HiRISE BG/RED), and 1.43 band depth (CRISM) for sites Cusco, Fabi, and Lima.

Site name	L_s	CO_2 grain size (mm)	Dust cont. halo (%)	Dust cont. surr. (%)	Dust size (μm)
Cusco	288	8–8.5	0.025 ± 0.001	0.026 ± 0.001	10
Fabi	288	8.5–9.5	0.02 ± 0.001	0.028 ± 0.001	9.0–10.0
Fabi	298	9.0–10.0	0.03 ± 0.005	0.03 ± 0.005	14.0–16.0
Lima	285	8.0–9.0	0.03 ± 0.005	0.03 ± 0.005	8.0–9.0
Lima	299	8.0–10.0	0.03 ± 0.005	0.05 ± 0.001	14.0–17.0
Lima	309	5.5–8.0	0.06 ± 0.005	0.08 ± 0.001	16.0–20.0
Lima	315	6.5–8.0	0.065 ± 0.005	0.085 ± 0.005	19.0–22.0

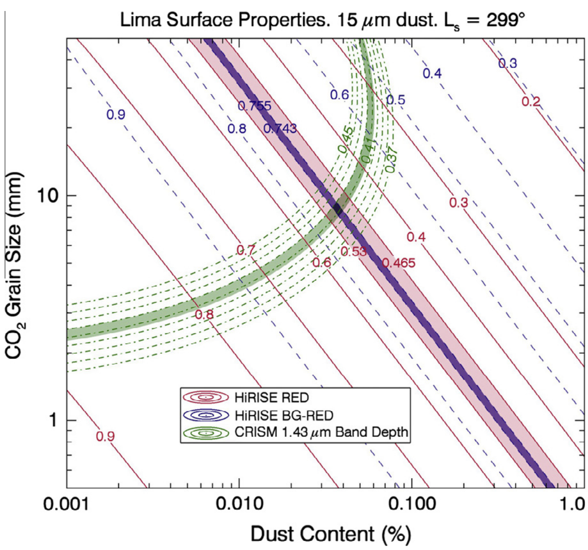

Fig. 11. Example of a contour map of surface photometric properties for the Lima site from our Hapke reflectance model. The shaded regions indicate the observed values of each of the three parameters (RED, BG/RED, 1.43 μm band depth) for this particular time of year (L_s 299°). The intersection of the shaded regions limits the composition of the surface to a particular combination of CO_2 grain size, dust content, and dust grain size. This particular map corresponds to 15 μm dust grains, which in this case produced the best fit to the observations.

halos disappeared in MY 28 (~L_s 325–331°) seems to indicate that they are being covered by new CO_2 frost condensing as the fall approaches.

The observation that the brightest sections of the halos were seen adjacent to sun-facing walls could imply that the maximum brightness changes position during a single martian day, as the Sun changes azimuth. However, the presence of the same albedo trend in images with no halos suggests that this is an ever-present characteristic of the terrain surrounding the pits, and not of the ephemeral halos.

We initially considered three possible scenarios to explain the appearance of halos: 1. They are a product of contamination by small impurities of water ice either within the halos themselves or in the surroundings. 2. The halos are a result of finer-grained CO_2 frost that is either being freshly deposited onto areas of the surface adjacent to scarps, or left exposed by lower sublimation rates at areas a few tens of meters from the scarp, compared to those farther away. 3. Halos appear because of a difference in dust content between pit-adjacent surfaces and the rest of the SPRC.

Analysis of CRISM spectra and band depth measurements ruled out the first two theories. As seen in Fig. 9a, the spectrum taken from a halo pixel is almost identical to that taken from a surrounding pixel. Both spectra show characteristic CO_2 ice absorption bands, and a lack of water ice bands, ruling out water ice contaminants. Fig. 9c shows that the band depths actually increase in areas adjacent to pit walls. In a pure CO_2 ice surface, this would mean that the halo areas are darker than their surroundings rather than brighter, and thus these data seem to rule out an explanation based on ice grain size.

We are thus left with the third possible scenario, which has dust as the central driver for the appearance of halos. The HiRISE color data support the theory that the halos are formed due to a dust-content difference between the ice on the halos and the ice elsewhere in the SPRC, indicated by bluer ice close to the pits. In addition, our Hapke model seems to indicate that a small difference in dust content would result in the observed albedo difference. A difference in dust content as small as two to three hundredths of a percent volume is capable of producing the albedo, color, and band depth differences observed between the halos and their surroundings. Therefore, from our spectral analysis and modeling we infer that the halos are a result of a widespread darkening of the SPRC, rather than local brightening. This darkening was somehow prevented from being as pronounced in areas close to scarp walls as everywhere else on the cap.

4.2. Conceptual model

The effect of general SPRC darkening with certain areas kept brighter has not been observed before or since MY 28, indicating that some unique event occurred during the summer of MY 28 that prompted the SPRC darkening and the appearance of halos around erosional scarps. The one major difference between the southern summer of MY 28 and other years is the presence of a near-perihelion (~L_s 252°) planet-encircling dust storm. Bonev et al. (2008) have shown that sublimation rates in the SPRC increased immediately after the dust storm occurred. In addition to this unusually vigorous sublimation, there is a higher amount of dust expected to be present in the near-surface atmosphere. With this in mind, we propose a formation model for the halos, which explains their unique appearance in MY 28, and is shown schematically in Fig. 12.

Solar incidence angles tend to be lower for slopes than for flat surfaces near the polar regions. Therefore, the sunlit walls of erosional pits and scarps have a higher peak CO_2 ice sublimation rate than the flat surrounding plains, which results in a sublimation-driven outflow of gas from the walls of the scarps. The peak daily sublimation rates happen at sun-opposing walls. During the time of year when halos were seen, these peak sublimation rates are about 4–5 times greater than the flat surface values. Because of the Sun's azimuthal motion however, all wall orientations have higher sublimation rates than flat surfaces at some point during the martian day. If at the time of year of the most vigorous sublimation (which would happen immediately after the walls defrost in the middle of southern summer, ~L_s 270°) there was also an unusual amount of dust being deposited onto the surface (as would be the case after a global dust storm) this "sublimation wind" would have prevented some of the atmospheric dust from depositing in areas near pit walls, leaving these sections "cleaner" relative to the surrounding SPRC ice. In MY 28, as dust continued to

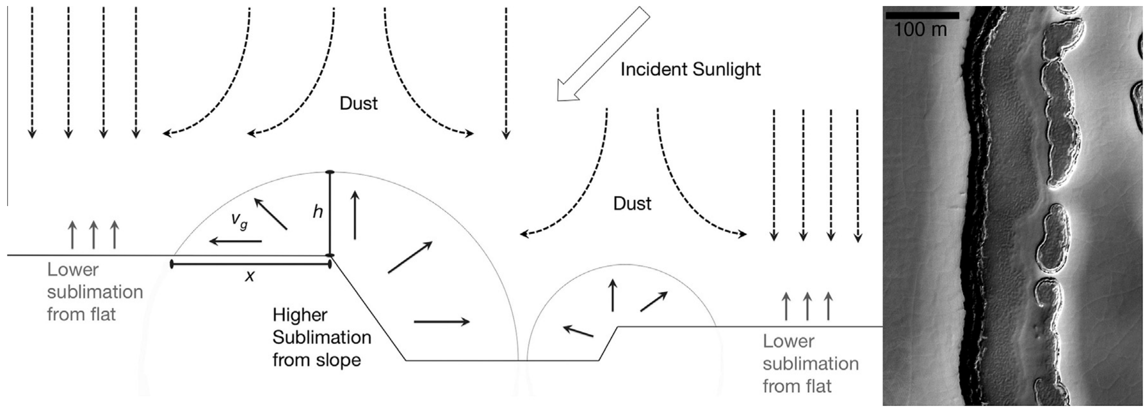

Fig. 12. Schematic of our conceptual model for the formation of SPRC halos (left). The higher sublimation rate on a slope due to lower solar incidence angles raises the partial pressure of CO_2 in the local near-surface atmospheric layer. This pressure difference creates a sublimation-driven outflow of gas that blows settling dust grains away from the slope and keeps areas near the edges of pits relatively dust-free with respect to the surroundings. Wherever steep opposing walls were observed, halos were seen atop both mesas (right: slice of PSP_004989_0945).

settle everywhere on the SPRC with increasing L_s, this process continued in areas close to the scarp. The result was that the entire cap, including the halo areas, was darker later in the year, but more dust was being prevented from settling in areas close to pit walls, so that the brightness difference between halos and their surroundings was enhanced (Fig. 5). In addition, it is likely that as time passed, early-deposited dust was removed from the surface immediately adjacent to the outer halo edges, resulting in an expanding halo area and wider observed halos (Fig. 5). Although this sublimation-driven effect occurs every year, MY 28 is the only year in the recent past in which a significant amount of dust was deposited during this season.

The distance a settling dust particle can be pushed away from a scarp wall should be proportional to the CO_2 sublimation rates calculated from a thermal model of the surface based on simple energy balance. Therefore, we can get an idea of the plausibility of the process described above by using modeled sublimation rates as a proxy for wind speed to deduce what size dust particles are required to form halos of about 33 m in width (average width of a halo in the middle of the halo season).

The settling of particles through a medium can be governed by turbulent flow, in which drag forces are caused by the deflection of the air stream around the particle, or by low-velocity laminar flow, in which viscous forces dominate and determine the drag (Melosh, 2011). The transition from one regime to another is defined by a dimensionless quantity known as the Reynolds number. In the case of a martian dust particle settling through a boundary layer of the atmosphere, we determined that laminar flow dominates (see Appendix B). Therefore, we use the Stokes' flow velocity (Melosh, 2011) for the laminar regime to estimate the settling velocity (v_s) of dust particles:

$$v_s = \frac{1}{18}\frac{(\sigma-\rho)d^2 g}{\eta} \tag{4.1}$$

Here, ρ is the atmospheric density (~0.02 kg/m^3), d is the dust grain size, η is the viscosity of the atmosphere (~1.3e−5 Pa s), σ is the density of the dust particle (~2700 kg/m^3), and g is the acceleration due to gravity on Mars (3.7 m/s^2). Typical Stokes' velocities for micron-sized particles are on the order of 4×10^{-5} m/s.

We assume that the particle is horizontally coupled to the gas and that it begins to be affected by the sublimation wind at a certain height (h) from the ground (Fig. 12). The time it takes the particle to fall to the ground by Stokes' flow (h/v_s), multiplied by the velocity of the sublimating gas (v_g) pushing the particle, should equal the distance traveled by the particle before it settles on the ice (x):

$$\frac{h}{v_s} v_g = x \tag{4.2}$$

This distance should therefore be comparable to the width of the halos, and increases as grain size decreases.

If we consider a surface area of 1 m^2 on the wall of a pit, and assume that half of the sublimated gas flows outward from the pit in every direction through a layer of thickness h (Fig. 12), then the velocity of the sublimating gas depends on the rate of sublimation of CO_2 from the wall (dm/dt):

$$v_g = \frac{1}{2}\left[\frac{\left(\frac{dm}{dt}\right)}{\rho}(h)^{-1}\right] \tag{4.3}$$

Combining Eqs. (4.1)–(4.3) and rearranging terms gives an expression for the particle size (d) required to form a halo of width x by this mechanism:

$$d = \sqrt{\frac{9\eta\left(\frac{dm}{dt}\right)}{\rho x g(\sigma-\rho)}} \tag{4.4}$$

Using a simple energy balance model, we calculated the CO_2 ice peak sublimation rates (dm/dt) for north and south-facing walls of various slope angles. Fig. 13 shows the changes in sublimation rate for a 50° slope. For the time the halos were observed, the modeled sublimation rate is ~0.0005 kg s^{-1} m^{-2}.

This sublimation rate is for a one square meter patch of ice from a wall. The walls on the SPRC pits are at least a few meters tall in most cases, so the sublimation rate can be ~5 times higher than the quoted value, which would make d about 2–3 times larger. However, it is likely that the real sublimation values are not exactly the daily peak rates that we use here. We use this value for the sublimation rate in Eq. (4.4), and find that the dust grain size necessary to produce 33 m halos at the current modeled sublimation rates is ~3 μm. This value is quite reasonable for martian atmospheric dust (Wolff and Clancy, 2003), but smaller than the grain sizes we found to be present on the surface from our reflectance model. The Hapke model is well suited to explore relative grain size differences and dust contents, but is less reliable for calculations of absolute grain sizes (Souchon et al., 2011; Zhang and Voss, 2011; Helfenstein and Shepard, 2011). In addition, spectroscopic grain sizes do not necessarily match physical grain sizes. We can therefore infer that the higher sublimation rates during the summer of MY 28 coupled

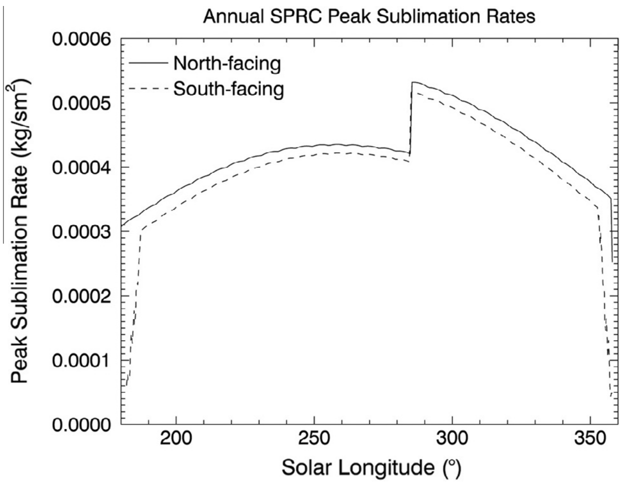

Fig. 13. Modeled sublimation rates for north (solid line) and south-facing (dashed line) slopes on the SPRC. The abrupt jump in sublimation rate at L_s 285° corresponds to the change in albedo due to the defrosting of the pit walls, which exposes older, darker ice.

with the dust settling from the atmosphere due to the midsummer global dust storm would be adequate conditions for halos to form.

Although this calculation has simplified reality in many respects, the broad agreement between the particle sizes, sublimation mass fluxes and halo widths shows this theory of halo formation to be reasonable.

4.3. Possibility of halos on other Mars years

Our work on the halos has shown that the residual cap darkened by up to 8% due to the dust storm, i.e. the halos were not due to local brightening. An 8% reduction in albedo is significant and may make the difference between net accumulation and net ablation for that year. HiRISE observations confirm that after the halo occurrence at the end of summer in MY 28, the residual cap defrosted more extensively than usual (Fig. 14). We suggest that the halos disappeared because they were covered by condensing seasonal CO_2 frost at the onset of fall. Fig. 25.4 in Titus et al. (2008) shows CO_2 ice accumulation beginning around L_s 330°, which is the time the halos begin to disappear, and they are completely gone by $\sim L_s$ 335°.

As was explained in the above sections, halos require settling dust to form and so are not expected in non-dust-storm years. Two other Mars years with global dust storms deserve special mention here. MY 9 had a late-southern-summer dust storm similar in timing to that of MY 28 and the Mariner 9 spacecraft observed the SPRC immediately afterward. The images show a variegated cap (Fig. 3 in Thomas et al. (2013)), with areas that are currently covered in frost all year appearing dark (Mariner 9 image resolution is too coarse to see decameter-size halos, but we expect them to have been present). The MY 9 appearance suggests that, like MY 28, there was also widespread defrosting in response to the dust storm. In MY 12 the Viking orbiters showed the cap had fully recovered, was again completely frosted (Fig. 3 in Thomas et al. (2013)) and appeared similar to generic non-storm years. HiRISE imagery shows a similar (but less severe) sequence of events on the residual cap after the MY 28 dust storm (Fig. 14): widespread thinning of frost was observed, was largely reversed one martian year later, and ice continued to accumulate over subsequent years.

The other special year is MY 25, which had a global dust storm during southern spring rather than southern summer. MOC was observing the residual cap at the time and no halos were observed that year. These observations may suggest that spring sublimation is too weak to create an outward flow of gas from the pit walls sufficiently strong to deflect falling dust grains i.e. halos did not appear because the cap was coated evenly with dust. This is consistent with thermal modeling, which shows slower sublimation rates from pit walls during the spring when they are covered with bright seasonal frost (Fig. 12).

4.4. Implications for mass-balance and history of the SPRC

What do the halos tell us about the mass-balance of the SPRC? The timing of their disappearance indicates that they most likely were buried by seasonal frost by the end of MY 28. There are other processes that could affect the albedo of the surface and manifest as the halos disappearing, but we consider these to be unlikely. Dust sinking into the ice could raise the albedo of the surface, thereby changing the albedo of the surroundings to that of the halos, and erasing the brightness difference. Although this process could be effective near solstice when insolation is high, the halos disappear in late summer, when incidence angle and insolation is low, and when new deposition is expected (Titus et al., 2008). Thermal metamorphism and ice pore infilling (Eluszkiewicz et al., 1993, 2005) could also have an effect on the surface albedo. However, there is no reason to assume that these processes would affect ice closer to pit walls differently than everywhere else on the cap, given that both areas are composed of CO_2 ice at the same temperature.

The fact that the halos were not exhumed during the late summer of MY 29 shows that the flat surfaces in the SPRC underwent net accumulation during MY 29. In addition, since they were not exhumed in any subsequent year, the net mass-balance over MY 29–31 was also positive. The situation on the SPRC in non-dust-storm years appears to be one of net accumulation on flat surfaces even while the steeply inclined walls of the pits retreat several meters per year through ablation.

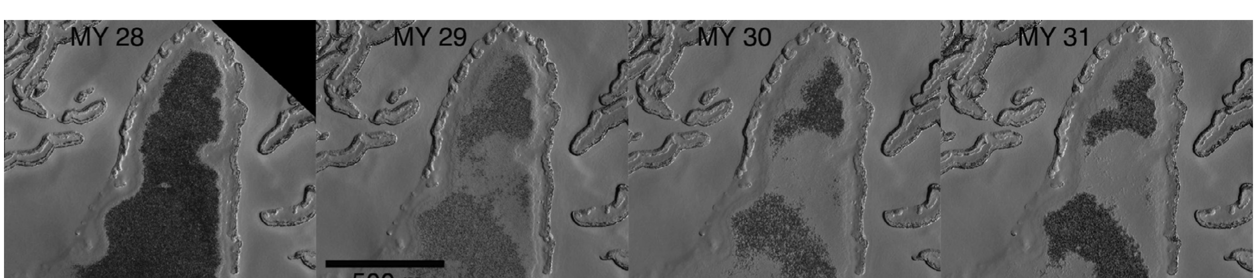

Fig. 14. Section of the SPRC at the Trujillo site during four different Mars years. Defrosting after the MY 28 dust storm and halos was more pronounced than in later years, meaning that the cap recovered from a year with stronger than usual sublimation rates.

MY 28 may have been a year of net ablation for flat surfaces, as the cap was darker. Modeling of the effects of near-solstice global dust storms also suggests that these events should lead to net ablation (Bonev et al., 2008). Nevertheless, the SPRC recovered in the following years (Fig. 14). It showed a similar recovery in the years after the MY 9 dust storm, evidenced by the fact that areas defrosted during Mariner 9 observations had re-frosted by MY 12 when observed by Viking. MY 25 saw a global dust storm near spring equinox (while seasonal accumulation was still in progress). However, MOLA radiometry observations show that the SPRC had a brighter appearance during summer of MY 25 compared to preceding and following years with no dust storms (Byrne et al., 2008), indicating that the MY 25 dust may have been buried in the seasonal frost and not exhumed in late summer, implying another year of positive mass balance.

One model of SPRC behavior (Byrne, 2011) suggests that flat surface accumulation and ablation of retreating pit walls is ongoing and leads to a transitory, but regenerating ice cap, in agreement with observations presented here. In that model, surface roughness leads to pit generation and a recovering SPRC becomes possible only if surface roughness is smoothed. Byrne (2011) speculate that these smoothing events are linked to enhanced snowfall in the winter that postdates global dust storms; this aspect of the model is consistent with, but not proven by, what has been presented here.

5. Summary and conclusions

The discovery and analysis of previously unknown albedo features on the martian SPRC, which we have dubbed "halos", was explained in detail. The SPRC darkened everywhere due to a global dust storm during late MY 28; however, sections of ice adjacent to the edges of erosional pits darkened to a lesser degree. We defined the SPRC halos to be these sections that remained relatively bright with respect to the rest of the cap. Analysis of HiRISE imaging shows that they are up to 8% brighter than the surrounding ice, and are larger when adjacent to equator-facing walls. In eight Mars years of observations, the halos were observed only during midsummer of MY 28 between L_s 280° and 330°, indicating a possible relationship between the appearance of these features and a global dust storm that occurred in MY 28 near martian perihelion (L_s 252°). This theory was investigated by analyzing IR spectra from the CRISM instrument, and color ratios from HiRISE. The spectra showed that both the halos and their surroundings are primarily composed of CO_2 ice, while the color ratios showed bluer ice in the halos, which is indicative of lower dust contents. Spectral modeling with Hapke theory confirmed that a self-consistent set of CO_2 ice grain sizes and dust contents can explain the albedo difference of the halos and their deeper CO_2 ice absorption bands. Although the halos have larger ice grain sizes (Fig. 10), they are deficient in dust, which makes them brighter and bluer than the surrounding ice. An analysis of the settling rates of dust particles in the martian atmosphere is consistent with settling dust particles being pushed away from halo zones by a sublimation-driven wind.

There are two important conclusions to be drawn from our work:

1. The single-time, ephemeral occurrence of the halos indicates that the layer of ice that darkened as a result of the dust storm and surrounded the halos, was not exhumed in subsequent years, implying a positive mass balance for flat surfaces on the SPRC during MY 29, and net positive mass balance from the end of MY 28 through the end of MY 31.
2. In order for halos to form on the SPRC, special conditions must be met that require the presence of an unusual amount of dust in the atmosphere at the correct time of year. This not only darkens the cap through the settling of dust, but also increases the sublimation rates through an increase in atmospheric heating (Bonev et al., 2008).

Our work clearly illustrates the importance of the continuous monitoring of the martian polar regions. Anomalous dust storm years like MY 28 may hold the key to the persistence of the South Polar Residual Cap and at a minimum have resolved the question of whether the flat surfaces of the cap are currently accumulating or not. The SPRC likely contains many dust layers from global dust storms that have occurred over its accumulation and may one day present an important historical record for core sampling.

Acknowledgments

We thank the HiRISE, CTX, MOC and CRISM teams for acquiring and processing the data used in our study. We also thank the JMARS development team at Arizona State University's Mars Space Flight Facility for their support during the use of their software. Research award number NNX09AM01G, from NASA's Mars Data Analysis Program (MDAP), funded this work. AJB participated in this work under NASA Contact NNX13AJ73G.

Appendix A. Hapke reflectance model

Hapke (2012) developed a series of equations to calculate the reflectance of a particulate surface given known properties and assumptions about the solid phases composing the surface based on Mie scattering theory. In the case of the SPRC, the mixtures composing the surface are intimate mixtures, and represent a surface in which the individual components exist as separate grains but are mixed at a scale fine enough for single photons to interact with both types of material. Our implementation of this model is largely based on the work of Roush (1994). We neglect atmospheric extinction and scattering in the calculation of the I/F values.

The spectral reflectance of an intimate mixture is based on the bidirectional reflectance, given by:

$$r(i,e,g) = \left(\frac{w}{4\pi}\right)\left(\frac{\mu_0}{\mu_0-\mu}\right)\{[1+B(g)]P(g)+H(\mu_0)H(\mu)-1\} \tag{A1.1}$$

where w is the average single scattering albedo of the mixture, and depends on composition and grain size, μ_0 is the cosine of the incidence angle i, and μ is the cosine of the emission angle e. $B(g)$ is the function describing the opposition surge, which we assume to be equal to zero since the phase angle of our observations is always greater than 50°. We assume isotropic scattering, and thus the phase function $P(g)$ is equal to 1. $H(\mu_0)$ and $H(\mu)$ are Chandrasekhar's (1960) H-functions, given by:

$$H(x) = \frac{1}{1-(1-\gamma)x\left[r_0+\left(1-\left(\frac{r_0}{2}\right)-r_0x\right)\ln\left(\frac{1+x}{x}\right)\right]} \tag{A1.2}$$

defined by the albedo factor: $\gamma=\sqrt{1-w}$, and the diffusive reflectance: $r_0=\frac{1-\gamma}{1+\gamma}$.

This approximation for the H-functions (from Eq. (8.57) of Hapke (1993)) was chosen because it estimates $H(x)$ more accurately for extremely bright surfaces.

As we assume that the dust and ice in the SPRC are intimately mixed, the average single scattering albedo for the mixture is given by Eq. (10.46) of Hapke (2012):

$$w = \frac{\left(\sum_j^n \frac{M_j Q_{S_j}}{\rho_j D_j}\right)}{\left(\sum_j^n \frac{M_j Q_{E_j}}{\rho_j D_j}\right)} \tag{A1.3}$$

where M_j, ρ_j, D_j are the mass fraction, solid density, and diameter of the jth particle, and n is the total number of components in the mixture. Brown et al. (2008) used a similar approach. Q_{Ej} is the extinction efficiency of the jth particle, which is equal to 1 for particles much larger than the wavelength, as is the case here (Eq. (7.41), Hapke (2012)). Q_{Sj} is the scattering efficiency of the jth particle, and is defined by:

$$Q_s = S_e + (1 - S_e)\frac{(1 - S_e)\Theta}{1 - S_e\Theta} \tag{A1.4}$$

S_e and S_i are the external and internal reflection coefficients:

$$S_e = \frac{1}{2}(|R_\parallel|^2 + |R_\perp|^2) \tag{A1.5}$$

S_i is defined by integrating the expression for S_e over all angles (excluding internal reflection). Where $R_\parallel$ and $R_\perp$ are the Fresnel reflection coefficients polarized parallel and perpendicular to the incident sunlight, respectively. These are given by:

$$|R_\perp|^2 = \frac{\left(\cos\left(\frac{g}{2}\right) - u\right)^2 + v^2}{\left(\cos\left(\frac{g}{2}\right) + u\right)^2 + v^2} \tag{A1.6a}$$

$$|R_\parallel|^2 = \frac{\left((n^2 - k^2)\cos\left(\frac{g}{2}\right) - u\right)^2 + \left(2nk\cos\left(\frac{g}{2}\right) - v\right)^2}{\left((n^2 - k^2)\cos\left(\frac{g}{2}\right) + u\right)^2 + \left(2nk\cos\left(\frac{g}{2}\right) + v\right)^2} \tag{A1.6b}$$

where

$$u = \sqrt{\frac{1}{2}\left(n^2 - k^2 - \sin\left(\frac{g}{2}\right) + \sqrt{\left(\left(n^2 - k^2 - \sin\left(\frac{g}{2}\right)\right)^2 + 4n^2k^2\right)}\right)} \tag{A1.7a}$$

and

$$v = \sqrt{\frac{1}{2}\left(-\left(n^2 - k^2 - \sin\left(\frac{g}{2}\right)\right) + \sqrt{\left(\left(n^2 - k^2 - \sin\left(\frac{g}{2}\right)\right)^2 + 4n^2k^2\right)}\right)} \tag{A1.7b}$$

The real and imaginary parts of the complex index of refraction for each component are n and k respectively, and taken from previous work (see Section 2.4).

Θ is the internal transmission coefficient of each particle:

$$\Theta = \frac{r_1 + \exp(-\langle D\rangle\sqrt{\alpha(\alpha + s)})}{1 + r_1\exp(-\langle D\rangle\sqrt{\alpha(\alpha + s)})} \tag{A1.8}$$

where r_1 is:

$$r_1 = \frac{(1 - \sqrt{\alpha/(\alpha + s)})}{(1 + \sqrt{\alpha/(\alpha + s)})} \tag{A1.9}$$

α is the absorption coefficient, which is related to the imaginary index of refraction and the incident wavelength through the dispersion relation:

$$\alpha = \frac{4\pi k}{\lambda} \tag{A1.10}$$

and s is the volume scattering coefficient, which we assume to be 10^{-17} for minimal internal scattering (Roush, 1994).

Finally, the mean photon path length D is related to the grain diameter D, and n and k by:

$$\langle D\rangle = \frac{2}{3}\left(n^2 - \frac{\sqrt{n^2 - 1}}{n}\right)D \tag{A1.11}$$

The bidirectional reflectance is then transformed to I/F by multiplying it by π (assuming isotropic scattering), and later to Lambert Albedo by dividing I/F by the cosine of the incidence angle (μ_0).

The model outputs I/F values for all wavelengths from 0.35 to 4 μm, at a resolution of 1 nm. This range encompasses all CRISM and HiRISE channels.

The final step in the model is to transform these I/F values to HiRISE and CRISM responses. To do this, we convolve the model I/F function with weighting factors for each band, which account for band response, quantum efficiency of the detector, solar spectrum, and mirror efficiency (Delamere et al., 2010; Murchie et al., 2007).

Appendix B. Flow regime calculations

The ratio of inertial to viscous forces, known as the Reynolds number, determines the transition from turbulent to laminar flow:

$$Re = \frac{\rho v d}{\eta} \tag{A2.1}$$

Here, ρ is the density of the atmosphere, v is the velocity of the particle relative to the atmosphere, d is the grain size of the particle, and η is the viscosity of the atmosphere. When this number is low, inertial forces are weak compared to viscous forces, and the laminar regime dominates over turbulence.

We calculated the terminal velocity of a test dust particle 10 μm in size settling in the martian atmosphere in both the turbulent and laminar regime, to evaluate the Reynolds number and decide on the correct value for the particle's velocity in our calculations.

The terminal velocity due to turbulent flow is given by:

$$v_t = \sqrt{\frac{4}{3}\frac{(\sigma - \rho)dg}{C_D\rho}} \tag{A2.2}$$

in which σ is the density of the dust particle, g is the acceleration due to gravity, and C_D is the empirical constant known as the drag coefficient (~0.4 for a sphere, over a wide range of velocities).

The terminal velocity in the laminar regime is given by the Stokes velocity:

$$v_s = \frac{1}{18}\frac{(\sigma - \rho)d^2g}{\eta} \tag{A2.3}$$

We used typical martian values for all the parameters in the above equations: $\rho = \sim 0.02$ kg/m^3, $d = \sim 10$ μm, $\eta = \sim 1.3\text{e}{-5}$ Pa s, $\sigma = (\sim 2700$ kg/m$^3)$, and $g = 3.7$ m/s^2.

Solving the two velocity equations gives $v_t = 4$ m/s and $v_s = 0.004$ m/s. Substituting these values into Eq. (A2.1) gives Reynolds numbers of 6×10^{-2}, and 6×10^{-6} respectively, both of which are significantly smaller than 1. Therefore, we can be confident that the settling of micron-sized dust particle on Mars is dominated by Stokes flow, and that Eq. (A2.3) is the correct expression to use.

Appendix C. Supplementary material

Supplementary data associated with this article can be found, in the online version, at http://dx.doi.org/10.1016/j.icarus.2014.04.050.

References

Bibring, J.P. et al., 2004. Perennial water ice identified in the south polar cap of Mars. Nature 428, 627–630.

Bonev, B.P., Hansen, G.B., Glenar, D.A., James, P.B., Bjorkman, J.E., 2008. Albedo models for the residual south polar cap on Mars: Implications for the stability of the cap under near-perihelion global dust storm conditions. Planet. Space Sci. 56, 181–193.

Brown, A.J., Byrne, S., Tornabene, L.L., Roush, T., 2008. Louth crater: Evolution of a layered water ice mound. Icarus 196 (2), 433–445.

Brown, A.J., Calvin, W.M., Mcguire, P.C., Murchie, S.L., 2010. Compact Reconnaissance Imaging Spectrometer for Mars (CRISM) south polar mapping: First Mars year of observations. J. Geophys. Res. 115, E00D13. http://dx.doi.org/10.1029/2009JE003333.

Brown, A.J., Calvin, W.M., Murchie, S.L., 2012. Compact Reconnaissance Imaging Spectrometer for Mars (CRISM) north polar springtime recession mapping: First 3 Mars years of observations. J. Geophys. Res. 117, E00J20. http://dx.doi.org/10.1029/2012JE004113.

Byrne, S., Ingersoll, A., 2003. A sublimation model for martian south polar ice features. Science 299, 1051–1053.

Byrne, S., Zuber, M.T., Neumann, G.A., 2008. Interannual and seasonal behavior of Martian residual ice-cap albedo. Planetary and Space Science 56, 194–211. http://dx.doi.org/10.1016/j.pss.2006.03.018.

Byrne, S., 2009. The polar deposits of Mars. Annu. Rev. Earth Planet. Sci. 37, 535–560.

Byrne, S., 2011. Simulating the landscape evolution of the martian residual CO_2 ice cap. Lunar Planet. Sci. 42. Abstract 2728.

Chandrasekhar, S., 1960. Radiative Transfer. Dover, New York.

Clancy, R.T. et al., 2000. An intercomparison of ground-based millimeter, MGS TES, and Viking atmospheric temperature measurements: Seasonal and interannual variability of temperatures and dust loading in the global Mars atmosphere. J. Geophys. Res. 105 (E4), 9553.

Clark, R.N., Lucey, P.G., 1984. Spectral properties of ice-particulate mixtures and implications for remote sensing. I – Intimate mixtures. J. Geophys. Res. 89, 6341–6348 (ISSN 0148-0227).

Cornwall, C., Titus, T.N., 2010. A comparison of martian north and south polar cold spots and the long-term effects of the 2001 global dust storm. J. Geophys. Res. 115 (E6), E06011.

Delamere, W.A., Tornabene, L.L., McEwen, A.S., Becker, K., Bergstrom, J.W., Bridges, N.T., Eliason, E.M., Gallagher, D., Herkenhoff, K.E., Keszthelyi, L., Mattson, S., McArthur, G.K., Mellon, M.T., Milazzo, M., Russell, P.S., Thomas, N., 2010. Color imaging of Mars by the High Resolution Imaging Science Experiment (HiRISE). Icarus 205, 38–52.

Eluszkiewicz, J., 1993. On the Microphysical State of the Martian Seasonal Caps. Icarus 103, 43–48.

Eluszkiewicz, J., Moncet, J.L., Titus, T.N., Hansen, G.B., 2005. A microphysically-based approach to modeling emissivity and albedo of the martian polar seasonal caps. Icarus 174, 524–534. http://dx.doi.org/10.1016/j.icarus.2004.05.025.

Hansen, G.B., 2005. Ultraviolet to near-infrared absorption spectrum of carbon dioxide ice from 0.174 to 1.8 μm. J. Geophys. Res. 110, E11003. http://dx.doi.org/10.1029/2005JE002531.

Hapke, B., 1993. Theory of Reflectance and Emittance Spectroscopy. Cambridge University Press.

Hapke, B., 2012. Theory of Reflectance and Emittance Spectroscopy, second ed. Cambridge University Press.

Hayne, P.O., Paige, D.A., Heavens, N.G.The Mars Climate Sounder Science Team, 2014. The role of snowfall in forming the seasonal ice caps of Mars: Models and constraints from the Mars Climate Sounder. Icarus 231, 122–130.

Helfenstein, P., Shepard, M.K., 2011. Testing the Hapke photometric model: Improved inversion and the porosity correction. Icarus 215, 83–100.

Kieffer, H.H., 1979. Mars south polar spring and summer temperatures – A residual CO_2 frost. J. Geophys. Res. 84, 8263–8288.

Leighton, R.B., Murray, B.C., 1966. Behavior of carbon dioxide and other volatiles on Mars. Science 153, 136–144.

Malin, M.C., Edgett, K.S., 2001. Mars Global Surveyor Mars Orbiter Camera: Interplanetary cruise through primary mission. J. Geophys. Res. 106 (E10), 23429–23570.

Malin, M., Caplinger, M., Davis, S., 2001. Observational evidence for an active surface reservoir of solid carbon dioxide on Mars. Science 294, 2146–2148.

Malin, M.C. et al., 2007. Context Camera Investigation on board the Mars Reconnaissance Orbiter. J. Geophys. Res. 112, E05S04. http://dx.doi.org/10.1029/2006JE002808.

McEwen, A.S. et al., 2007. Mars Reconnaissance Orbiter's High Resolution Imaging Science Experiment (HiRISE). J. Geophys. Res. 112, E05S02. http://dx.doi.org/10.1029/2005JE002605.

Melosh, J.H., 2011. Planetary Surface Processes. Cambridge University Press.

Murchie, S. et al., 2007. Compact Reconnaissance Imaging Spectrometer for Mars (CRISM) on Mars Reconnaissance Orbiter (MRO). J. Geophys. Res. 112, E05S03. http://dx.doi.org/10.1029/2006JE002682.

Roush, T., 1994. Charon: More than water ice? Icarus 108, 243–254.

Souchon, A.L., Pinet, P.C., Chevrel, S.D., Daydou, Y.H., Baratoux, D., Kurita, K., Shepard, M.K., Helfenstein, P., 2011. An experimental study of Hapke's modeling of natural granular surface samples. Icarus 215, 313–331.

Thomas, P.C. et al., 2000. North–south geological differences between the residual polar caps on Mars. Nature 404, 161–164.

Thomas, P.C., Malin, M.C., James, P.B., Cantor, B.A., Williams, R.M.E., Gierasch, P., 2005. South Polar Residual Cap of Mars: Features, stratigraphy, and changes. Icarus 174, 535–559.

Thomas, P., James, P., Calvin, W., Haberle, R., Malin, M., 2009. Residual south polar cap of Mars: Stratigraphy, history, and implications of recent changes. Icarus 203, 352–375.

Thomas, P.C., Calvin, W.M., Gierasch, P., Haberle, R., James, P.B., Sholes, S., 2013. Time scales of erosion and deposition recorded in the residual south polar cap of Mars. Icarus 225, 923–932.

Titus, T.N., Kieffer, H.H., Christensen, P.R., 2003. Exposed water ice discovered near the South Pole of Mars. Science 299, 1048–1051.

Titus, T.N., Calvin, W.M., Kieffer, H.H., Langevin, Y., Prettyman, T.H., 2008. Martian Polar Processes, Chapter 25 in The Martian Surface: Composition, Mineralogy, and Physical Properties, ed. Jim Bell. Cambridge University Press.

Warell, J., Davidsson, B.J.R., 2010. A Hapke model implementation for compositional analysis of VNIR spectra of Mercury. Icarus 209, 164–178.

Warren, S.G., 1984. Optical constants of ice from the ultraviolet to the microwave. Appl. Opt. 23 (8), 1206–1225.

Wolff, M.J., Clancy, R.T., 2003. Constraints on the size of Martian aerosols from Thermal Emission Spectrometer observations. J. Geophys. Res. 108 (E9), 5097. http://dx.doi.org/10.1029/2003JE002057.

Wolff, M.J. et al., 2009. Wavelength dependence of dust aerosol single scattering albedo as observed by the Compact Reconnaissance Imaging Spectrometer. J. Geophys. Res. 114, E00D04. http://dx.doi.org/10.1029/2009JE003350.

Zhang, H., Voss, K.J., 2011. On Hapke photometric model predictions on reflectance of closely packed particulate surfaces. Icarus 215, 27–33.